© Indian Academy of Sciences

Photocatalytic degradation of textile dyeing wastewater under visible light irradiation using green synthesized mesoporous non-metal-doped TiO$_2$

ELSAYED T HELMY[1], **AHMED EL NEMR**[1], **ESAM ARAFA**[2], **SHADY ELDAFRAWY**[2] **and MAHMOUD MOUSA**[3,*]

[1]Environment Division, National Institute of Oceanography and Fisheries, KayetBey, Elanfoushy, 55621 Alexandria, Egypt
[2]Chemistry Department, Faculty of Science, Mansoura University, 35516 Mansoura, Egypt
[3]Chemistry Department, Faculty of Science, Benha University, 13511 Benha, Egypt
*Author for correspondence (mousa_chem@yahoo.com)

Abstract. Because of simplicity, eco-friendly and attracting of scientific community, pure and non-metal-doped TiO$_2$ nanoparticles (NPs) photocatalysts: TiO$_2$ (T), C-TiO$_2$ (CT), N-TiO$_2$ (NT), S-TiO$_2$ (ST) and C, N, S-TiO$_2$ (CNST) were prepared by aqueous mangrove extract via sol–gel method. The materials were characterized by XRD, FTIR, UV–Vis absorption spectroscopy, BET, SEM, TEM, EDX, XPS, EIS and PEC. The results indicated that the planned photocatalysts exhibit an anatase crystal phase with a particle size in the range of 20–37 nm. The non-metal doping induces a redshift of optical absorption edge, and exhibits a strong visible light absorption. The photoluminescence intensity emission follows the order: T > CT > ST > NT > CNST, whereas the photocatalytic activity (PCA) increases in the reverse order. The PCA was assessed by photodegradation of two organic dyes, reactive blue 19 (B19) and red 76 (R76) under visible light illumination. The enhancement in visible PCA followed the order CNST > NT > ST > CT > T. The photocatalytic degradation efficiency of the dyes using the CNST sample reached 100% after 60 min of irradiation. The most active species in the photocatalytic processes are the positive holes. The solid photocatalysts were recycled five times without losing its activity. The chemical oxygen demand test confirmed that the CNST is the best photocatalyst of the investigated samples. Overall, the greenly synthesized NPs demonstrated the outstanding potential of green product for treating contaminated water by both B19 and R76 dyes under visible light illumination.

Keywords. TiO$_2$ doping; green synthesis; mangrove; photocatalytic degradation; wastewater treatment.

1. Introduction

Semiconductors are used to degrade organic pollutants in water to less harmful inorganic material [1]. There have been numerous studies carried out across the globe focussing on the decolourization of wastewater [2–7]. The importance of these types of research is increased in recent times and has become a subject of major public health concern and scientific interest.

Owing to the excellent properties of TiO$_2$, such as low-cost, non-toxicity, chemical stability and high photocatalytic activity (PCA), it has been considered as one of the good photocatalysts [4–7]. But, TiO$_2$ photocatalyst is realized to have some restrictions for sound applications. One of these restrictions is that TiO$_2$ has photocatalytic action only under ultraviolet radiation due to its high band gap

energy (E_g = 3.2 eV) [8–10]. This high value reduces the employment of sunlight as a source for excitation energy [9,10]. To rise above this problem, the photocatalytic activity of TiO$_2$ can be developed by decreasing its grain size and increasing its surface area, as well as by doping with metals and non-metals. Doping reduces the E_g through coupling the doping energy level of the doped ions with that of TiO$_2$ or an electronic coupling effect between doping ion and TiO$_2$ or produce some level of energy impurity between the conduction and the valence bands of TiO$_2$.

A wider range of approaches was employed for the preparation of the TiO$_2$ photocatalyst, such as hydrothermal, gas phase, microwave-assisted, solution combustion, solvothermal, sol–gel and green synthesis [11–17]. The green synthesis process is an eco-friendly technique because of the use of plant, bacteria, fungi or enzyme extracts for the

synthesis of TiO_2 NPs instead of the use of a large number of hazardous chemicals towards humans and the environment. Moreover, green synthesis of NPs provides more advantages over both physical and chemical methods because it is an easy process, very cost-effective and scalable for large-scale production, not requiring high pressure, high temperatures and costly equipment. The sol–gel is also one of the records encouraging techniques for the synthesis of doped TiO_2 NPs; it has several advantages than that of the other conventional processes, like the easier handling, very good homogeneity, controlling size, morphology and porosity particle properties.

The aim of the work in hand is to study the role of non-metal doping (C, S, N) on the crystallite size, optical absorption, E_g and PCA of the organized doped-TiO_2. The prepared materials were characterized by XRD, EDX, SEM, TEM, FTIR, UV–visible spectroscopy, photoelectric current, electrochemical impedance spectroscopy (EIS) and photoluminescence (PL) techniques. The PCA of the synthesized catalysts was determined through the degradation of textile organic dyes B19 and R76 effluents under the illumination of visible light.

2.   Materials and methods

2.1   Chemicals

Titanium tetra-isopropoxide (97%), isopropanol, sulphuric and nitric acids (analytical reagents, Sigma-Aldrich), urea, glucose monohydrate and thiourea were obtained from Fluka and all materials were used as received without any further purification. The double-distilled water was used in all the experiments.

2.2   Mangrove leaves extract preparation

Mangrove leaves were collected, washed with double-distilled water and left to dry in air for about 24 h before crushing in a manual mill. One litre of double-distilled water was dropped into 10 g of the powdered mangrove leaf in a beaker and kept stirring for 24 h at 318 K. The dark green colour extract was filtered using Whatman filter paper (No. 1) and stored at 277 K to avoid degradation or polymerization of sensitive phytochemicals before further use.

2.3   Nanoparticles synthesis

Synthesis of pure and doped TiO_2 was done by a conventional sol–gel method in mangrove aqueous extract solution. The pure TiO_2 sample was prepared by adding 80 ml of titanium tetra-isopropoxide solution drop by drop into a beaker containing 50 ml aqueous extracted mangrove under constant stirring at 323 K for 1 h and kept stirring at 323 K for 7 h to get the viscous gel. Thereafter, the gel obtained was heated at 673 K for 2 h in a muffle furnace. The same method was used to prepare ST, but with the addition of 10 ml of 15 wt% (1.33 M) H_2SO_4. The CT powder was obtained by adding 1.0 g of the prepared TiO_2 and 1 g glucose into 70 ml of aqueous mangrove and heating in an autoclave at 423 K for 12 h and finally cooled to room temperature in air. The produced CT powder was collected and washed several times with water and ethanol, followed by calcination in a muffle furnace at 673 K for 2 h. The NT was prepared by the same method mentioned for CT sample, but using 2 g urea in 100 ml aqueous mangrove instead of glucose solution. For the preparation CNST sample, we used 2 g of thiourea instead of urea.

2.4   Samples characterization

The synthesized photocatalysts were characterized by SEM using JEOL JEM-100CX II and TEM, JEOL-2010 techniques. The samples were prepared by ultrasonic dispersing of the powders as slurry in 2-propanol and deposited in TEM grids, XPS using (ULVAC PHI 5600, Chigasaki, Japan) AlKα radiation and XRD analysis using CuKα with $\lambda = 0.154$ nm radiation (Rigaku RINT2000, Tokyo, Japan). Scherrer formula was used to calculate the crystallite size from X-ray line broadening analysis [18]. N_2 adsorption–desorption analysis at 77.15 K was done using a Micromeritics ASAP 2020 instrument to estimate the surface data. UV–visible diffuse reflectance spectroscopy (DRS) was employed to study the optical properties of the powdered samples by using Shimadzu UV3150, Kyoto, Japan, and FTIR absorption spectra were recorded on Shimadzu FTIR8300, Kyoto, Japan; using KBr pellet. XPS experiments were carried out on an RBD upgraded PHI-5300 ESCA system (Perkin-Elmer) with a monochromatic MgKα excitation. The dopant concentration was analysed by XPS. The photoanodes were organized by making a thin film of ∼15 μm of photocatalyst on fluorine tin oxide (FTO) glass by using a paste from the photocatalyst materials with tert-butanol alcohol. Then, at 473.15 K, heating of the film paste was done for 3 h. PEC measurements were carried out in electrochemical cell consisted of the prepared photoanode, a counter electrode (Pt wire), a saturated calomel electrode (SCE) reference electrode and 1 M KOH solution. The electrodes were connected with a potentiostat system (PGSTAT204) for the PEC measurements. The electrodes were irradiated by a 500 W Xe lamp that was fitted with a cut-off filter (L-42, Hoya) for stopping the light in the UV region (400 nm $< \lambda <$ 800 nm). The light illumination was measured and it is equal to 100 mW cm^{-2}. EIS measurements were carried out under the open circuit condition at a frequency range between 0.01 Hz and 100 kHz.

2.5 *PCA evaluations*

The PCA was evaluated by measuring the decomposition of B19 and R76 textile dyes in aqueous solutions under visible light. The photocatalytic reaction was carried out in 200 ml cylindrical borosilicate-glass using Xenon lamp with properties mentioned in the above section as the visible light source. The lamp was fixed at a distance of 10 cm from the dye solution surface. The suspended dye solution (100 ml) containing the appropriate quantity of prepared NPs was continuously stirred in the dark to obtain equilibrium; after which the solution irradiated by visible light. Three millilitres of the irradiated suspended solution was then withdrawn at different time intervals and centrifuged at 50,000 rpm for 5 min. The dye optical absorbance of the supernatant liquid was determined at wavelengths of 592 and 542 nm for B19 and R76, respectively, using Shimadzu UV-2450 spectrometer (Shimadzu, Santa Clara, CA, USA). The degradation efficiency (η) of the photocatalyst was evaluated using the following equation:

$$\eta = \frac{(A_0 - A_t)}{A_0} \times 100\%, \tag{1}$$

where A_0 is the initial absorbance of the dye before mixing with the catalyst and A_t is the absorbance of the dye at a given reaction time t. The concentrations of the B19 and R76 textile dyes in industrial wastewater were calculated from calibration curves of optical absorption intensity *vs.* concentration. Chemical oxygen demand (COD) was estimated before and after the treatment of textile wastewater using potassium dichromate/sulphuric acid during a 2 h silver-catalysed oxidation at 420 K [18]. Based on the COD values obtained, the degradation efficiency (η) is calculated according to:

$$\eta = \frac{COD_o - COD_f}{COD_o} \times 100, \tag{2}$$

where η is the percentage of COD removal, while COD_o and COD_f are the measured COD values, before and after the photocatalytic treatment of wastewater, respectively.

3. Results and discussion

XRD patterns of the as-synthesized samples are shown in figure 1. The XRD of pure TiO_2 sample show only the characteristic peaks of anatase structure: (101), (004), (200), (105) and (204) with 2θ values at 25.2, 37.8, 48.0, 54.9 and 62.4 (JCPDS card no. 21-1272). However, the XRD of the doped photocatalysts displayed a slight shift in the peak positions to lower the θ values than the corresponding values for the pure TiO_2 (figure 1). The main characteristic (101) plane shifted with about 0.07° referring to the introduction of the doped ions into TiO_2 lattice. The sharpness of the peaks and the absence of unidentified peaks confirmed the crystalline nature and high purity of NPs
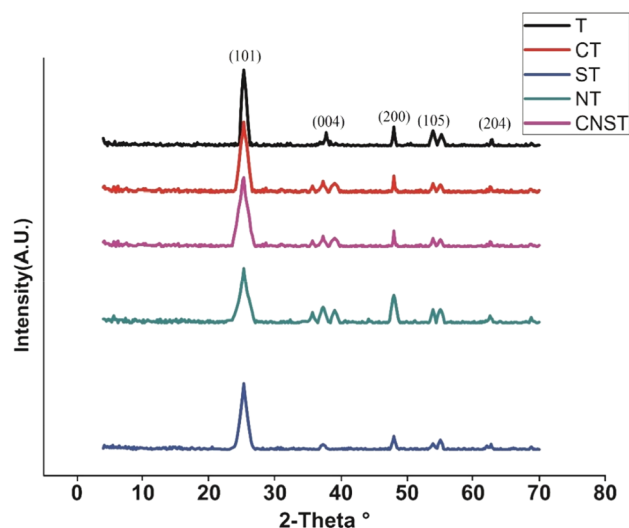
Figure 1. XRD of pure and doped TiO_2 samples.
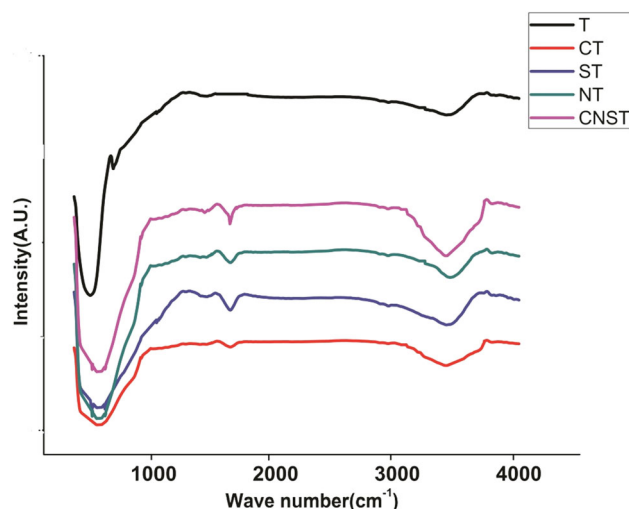
Figure 2. ATR–FTIR of the investigated samples.

prepared. The average crystal sizes (d_{XRD}) were estimated from XRD data using Scherrer's equation [19]:

$$d_{XRD} = 0.9\lambda / \beta \cos\theta, \tag{3}$$

λ is the X-ray wavelength (1.54 Å) and β (FWHM) is the full width at half maximum of the diffraction lines. The crystallite sizes of samples were different due to difference in its atomic radius, the d_{XRD} was found to be 37, 31, 29, 24 and 20 nm for T, CT, ST, NT and CSNT, respectively.

The ATR–FTIR spectrum analysis was performed to specify the functional groups present in pure and doped TiO_2 (figure 2). It shows intensive and wide bands at wavenumber below 1200 cm^{-1} due to the stretching vibrations of Ti–O and Ti–O–Ti bonds [20]. The absorption peaks observed at $\sim$1625 cm^{-1} in the spectra of NT and CNST samples were attributed to the stretching vibration of the N–H group [21]. Whereas the bands appeared at 1125, 1035 cm^{-1} are assigned to Ti–O–N and hyponitrite groups

found in N–TiO$_2$ and CNST samples. And the peaks observed at 1417 and 1050 cm^{-1} attributed to the nitrogen atoms embedded in the TiO$_2$ network [22]. The band appearing at 1035 cm^{-1} in the samples containing carbon is assigned to the vibration of the Ti–O–C bond and the peaks noted at 1389 and 1730 cm^{-1} are attributed to C–O stretching in carbonyl group [23]. The FTIR peak appeared at 1047 cm^{-1} for the samples containing sulphur is assigned to the Ti–O–S bond [24]. For each sample, a peak observed at 3200–3500 cm^{-1}, which is explained based on the bending and stretching vibrations of surface –OH group from surface absorbed water [25]. Remarkably, the intensity of the adsorbed water band in the undoped TiO$_2$ is stronger than that observed in the doped samples. This refers to that the doped samples contained more molecules of surface-adsorbed water and hydroxyl (OH) groups, which can play an important part in the photocatalytic reaction. Where the OH groups can arrest the photo-induced positive holes (h$^+$) produced by light irradiation to produce the high oxidizing hydroxyl radicals (OH$^\bullet$). Moreover, the surface OH$^-$ groups can proceed as absorption locations for oxygen molecules to form $^\bullet$OH$^-$ radicals leading to improve the PCD.

The photo-absorbance properties of the studied samples were studied using the UV–Vis diffuse reflectance spectra at wavelengths of 200–800 nm and the results obtained are illustrated in figure 3. The dopant ions shift the absorption edge toward longer visible-light wavelengths. The energy band gap value (E_g) for the investigated samples were calculated according to Tauc by using the following equation [26]:

$$(hvf(R))^n = A(hv - E_g), \tag{4}$$

where h is the Planck's constant, hv the photon energy, v the frequency of vibration, $f(R)$ the Kubelka–Munk function, A the proportional constant and exponent n has values depending on the nature of the transition. $n = 1/2$ for direct allowed transition and $n = 2$ for indirect allowed transition. Supplementary figure S1 represents the Tauc plot of $(hvf(R))^n$ *vs.* photon energy (hv) [26] for all the samples investigated. The E_g was decided from the extrapolation of the linear fit for the Tauc plot onto the energy axis and found to be 3.33, 3.16, 2.66, 2.36 and 2.18 eV for T, CT, ST, NT and CNST, respectively. In summary, the doping process causes structural defects of crystal lattice to introduce impurity or defect energy level and induces the local states below the conduction band edge and then, results in this redshift and narrows the band gap.
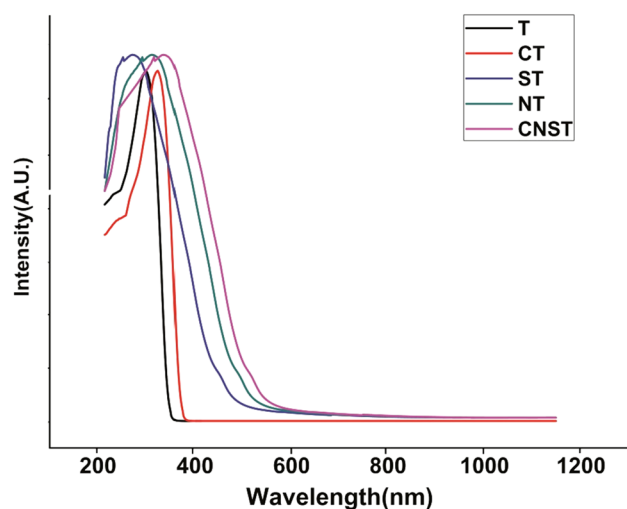
Figure 4 shows the PL emission spectra of the pure and doped samples. Each sample shows a clear blue–green emission band at ~ 2.6 eV. It is attributed to the transfer of the charge from Ti^{3+} to O^{2-} in a [TiO$_6$]$^-$ complex. This is linked with oxygen vacancies present on the surface of the sample. This reveals that the emission band originates from the intrinsic state instead of the surface state. The luminescence intensity has been found to increase in the order: T > CT > ST > NT > CNST. The PL emission is directly related to the recombination of excited electrons (e$^-$) and positive holes (h$^+$), the decrease in the rate of recombination implies that a large number of electrons and photo-generated gaps are involved in the photochemical transformation, In addition, the doped ions could enter into the lattice of TiO$_2$ and produce the shallow trapper, promoting the lifetime of carrier and reducing the recombination of electrons and holes effectively. Therefore, it is concluded that the presence of doped non-metals could be effective to enhance the photovoltaic performance of TiO$_2$, therefore, the lower PL intensity indicates a delay in recombination rate and, accordingly, higher photocatalytic activity [27].

EDX spectroscopy analyses of the studied samples are shown in supplementary figure S2a–d which reveal the presence of both (Ti, 4.508 keV) and (O, 0.525 keV) in all samples besides signals of (C, 0.277 keV) in CT sample,

Figure 3. Diffuse reflectance spectra of the investigated pure and doped samples.
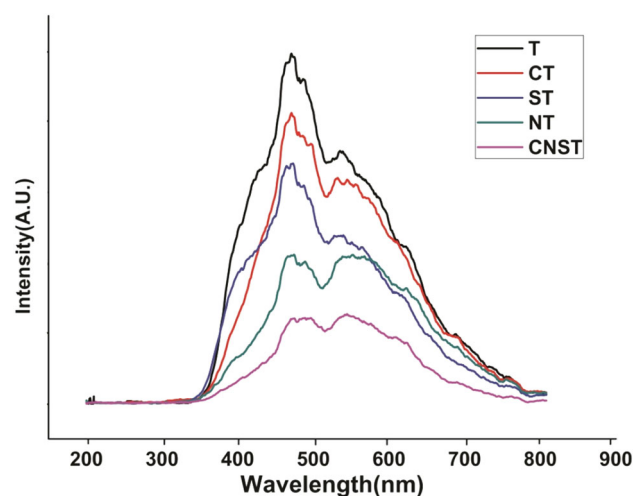
Figure 4. PL spectra of the investigated samples.

(S, 2.309 keV) in ST sample, (N, 0.392 keV) in NT sample as well as C, N and S in CNST sample. The outcomes improve the incorporation of the dopant into TiO_2 lattice.

To study the chemical states of the dopant elements integrated into TiO_2 lattice, the binding energies (BE) of Ti 2p, O 1s, C 1s, N 1s and S 2p core levels were investigated using high-resolution XPS spectra and the results obtained are represented in figure 5a–e. Figure 5a shows that the Ti $2p^{3/2}$ and Ti $2p^{1/2}$ core levels of pure TiO_2 appear at 458.8 and 464.5 eV due to O–Ti–O bonds in TiO_2 [28], whereas the corresponding peaks for doped samples appear at lower BE values indicating that the TiO_2 lattice is significantly
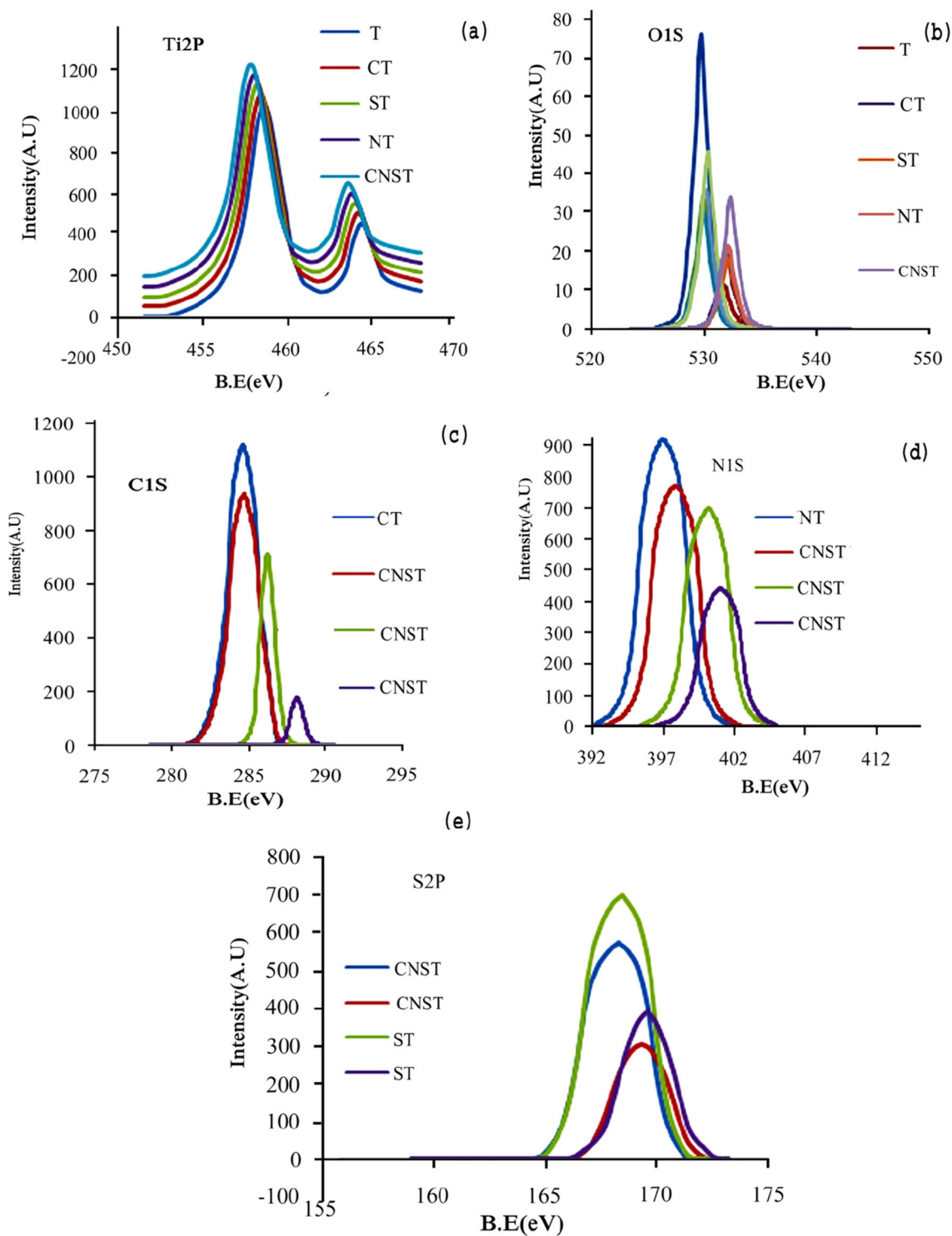
Figure 5. XPS spectra for Ti 2p; O 1s; C 1s, N 1s and S 2p core levels for the investigated samples.

modified by the C, N and S dopant elements. The shifts in the BE values indicate that the electronic interaction between Ti and the anions in doped TiO_2 is not the same as that in pure TiO_2. The XPS spectra of O 1s for pure and doped TiO_2 samples are given in figure 5b. The O 1s of the pure sample showed two peaks at BE of 529.6 and 531.5 eV. The related peaks for doped samples observed at lower BE than those of pure sample. The lower BE peak is essentially ascribed to the O–Ti–O bond in the TiO_2 lattice, and the higher BE peak is strongly connected to the $^{\bullet}OH^{-}$ groups produced principally from chemisorbed water. The XPS spectra of the C 1s core level of the CT and CNST samples are given in figure 5c. The CT shows one peak at 284.6 eV characterized for carbon element existing on the surface of TiO_2 as reported in other works [29]. Whereas the CNST sample shows three peaks: one at 284.7 eV characterized for carbon on the surface besides two other peaks at 286.2 and 288.8 eV characterized for C–O and C=O bonds, respectively [30]. Figure 5d shows the N 1s core level feature for CNST and NT. The peak observed at BE of 397.0 eV for the NT indicates the creation of N–Ti–O bonds, which refers to the substitution of N-ion for O-ion and the formation of N 2p states on the top of the VB on NT material and hence, a narrowing of the energy gap between the state of highest occupied and the state of lowest unoccupied [31]. The XPS spectrum of the CNST sample shows three peaks for N 1s at BE of 397.9, 400.2 and 401.2 eV. The high-intensity peaks detected above 400 eV are appointed to NO_2^{-} and NO_3^{-}. Other researchers reported that the 400 eV of the intense peak was due to nitrogen oxidized like Ti–N–O or Ti–O–N bonds [32,33]. S 2p XPS spectra for ST and CNST samples are illustrated in figure 5e. S 2p spectra of each sample showed two peaks in the BE range between 168.1 and 169.7 eV related to S $2p^{3/2}$, S $2p^{1/2}$ states [34], which reveal that S was introduced as S^{6+} ion. The introduction of S into TiO_2 lattice can also be validated by the drop in BE of the Ti $2p^{1/2}$ and Ti $2p^{3/2}$ of both the ST and CNST samples compared to the corresponding BE of Ti $2p^{1/2}$ and Ti $2p^{3/2}$ for the pure TiO_2 (figure 5a). This can be explained based on the difference in ionization energy of Ti and S. Thus, it can be deduced that the TiO_2 lattice was substituted by S^{6+} and created as a new energy level in the samples containing sulphur. The approximate dopant concentrations of the doped samples were determined from the doped element peak areas from the survey scans. The dopant concentration was found to be: 1.5 at% N for NT, 1.4 at% S for ST and 0.5 at% N and 0.9 at% S for CNST sample. The concentration of carbon is not calculated due to uncertainty.

The surface and morphology of the investigated samples were studied using SEM and TEM techniques. The micrographs obtained are presented in figure 6. The images of all samples showed agglomeration of smaller particles with almost deformed spherical shapes indicating that the shape of the NPs did not affect by changing the type of dopant element. It should be mentioned here that the SEM images of all the samples, except the ST sample, show rough surfaces with a large number of pores which are important characters for the photocatalytic process. The particle sizes of T, CT, ST, NT and CSNT samples are found to be 40, 30, 28, 11 and 18 nm, respectively, which agree well with those found by the XRD method.

The specific surface areas and pore volumes of the studied samples are shown in supplementary figure S3 and the results are summarized in table 1. All samples show a relatively high surface area due to their nanosized particles, which show that the surface area was improved by doping process, which might be caused by restrained growth of T in the presence of doped elements. It is known that materials with higher surface areas provide better photocatalytic efficiency in terms of surface reaction performance by providing more reaction sites. The pore volume of T also increased after doping process with the values observed at 0.17, 0.27, 0.22, 0.29 and 0.37 $cm^3 \ g^{-1}$ for T, CT, ST, NT and CNST, respectively, which were decreased after photocatalytic degradation process as in table 1.

EIS measurement is a powerful tool for studying the interfacial properties between electrodes and solution [35]. Figure 7a presents the Nyquist plots for the investigated samples under the illumination condition. It is observed that by introducing the doped elements, the semicircle in the plot became shorter, which indicates a decrease in the interface layer resistance and the charge transfer resistance on the surface. It is generally assumed that the smaller arc radius on the EIS Nyquist plot suggests a more effective separation of the photogenerated electron–hole pairs and a faster interfacial charge transfer. It means that the charge carriers that separate and transfer, are more effective in the doped samples, which lead to the significant enhancement of the photocatalytic capacity of the doped samples. In the doped TiO_2 samples, the oxygen sites were partially replaced by dopant atoms, while TiO_2 was simultaneously reduced. This causes the formation of an oxygen vacancy and a reduction of Ti^{4+} to Ti^{3+}, which act as a hole trap. While the electrons and holes are generated in the initial stage of visible light illumination, the defects produced on the TiO_2 surface or in the bulk can suppress the recombination of electron–hole pairs and hence, extend their lifetime [33–37]. As a result, the photocatalytic efficiency of the doped TiO_2 samples will be enhanced compared to the undoped sample.

Figure 7b, c shows the photocurrents produced by the illumination of the pure and doped TiO_2 NPs thin films deposited on FTO conducting glass substrates under dark and visible light. The potential was swept from 0 to 1.2 V_{SCE} at 5 mV s^{-1} scan rate. A small dark current density of a value < 2 mA cm^{-2} was recorded for each studied sample at the whole bias potential used. Whereas the light illumination caused a significant rise in the recorded current. This behaviour is a feature of n-type semiconductor and is attributed to photo-generated electrons diffusion through the counter electrode towards the
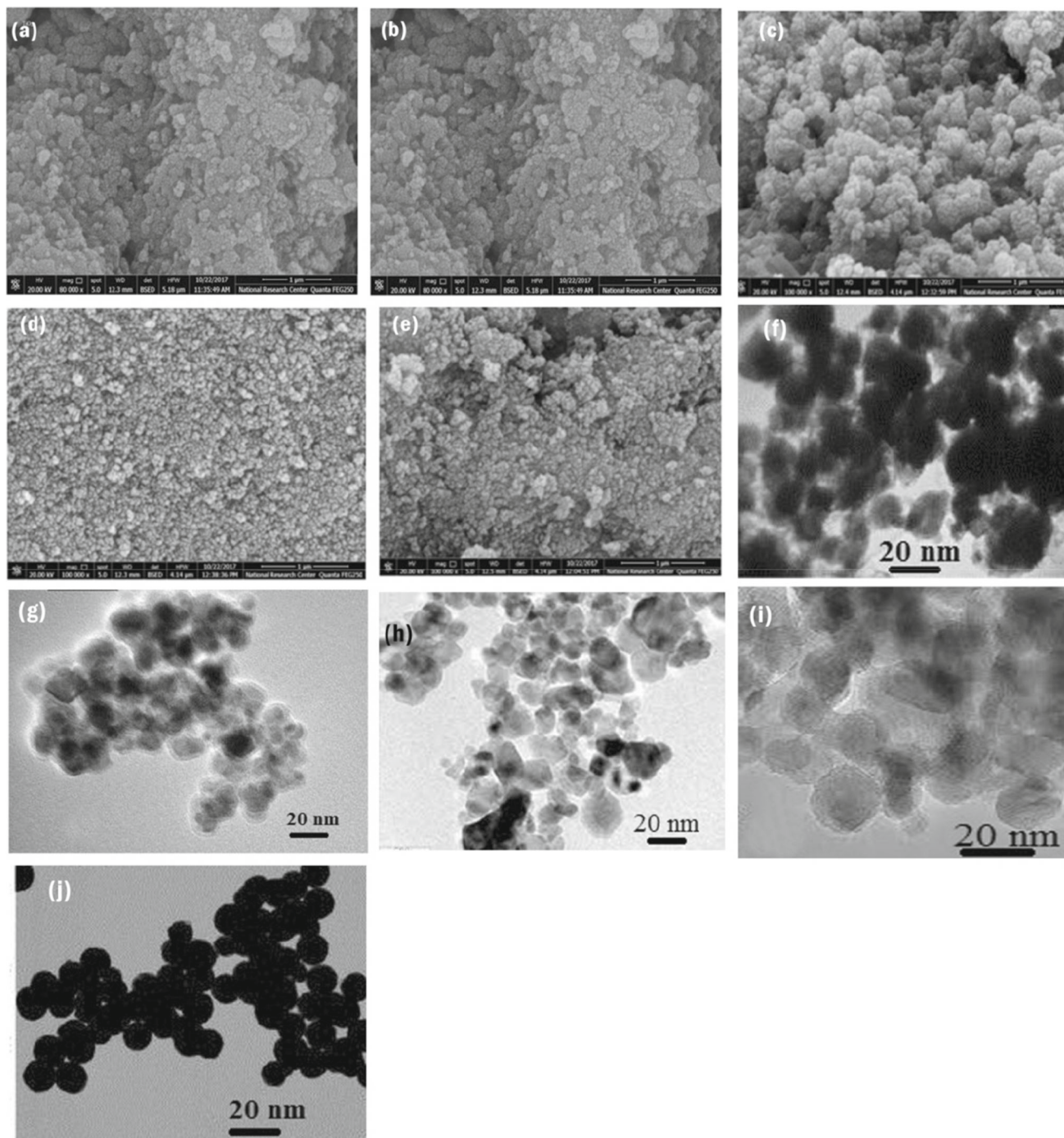
Figure 6. (**a–e**) SEM images for T, CT, ST, NT and CNST samples, respectively, and (**f–j**) TEM images for T, CT, ST, NT and CNST samples, respectively.

cathode. The detected anodic photocurrent might be associated with the production of $^{\bullet}OH$ and other oxidation products (e.g., H_2O_2) at the surface of TiO_2 electrodes, as will be seen later. The photocurrent increases according to: CNST > NT > ST > CT > T.

This reveals that the photogenerated e–h pairs were separated more effectively in CNST compared to other doped samples.

To determine the most photoactive material, the PCA of the prepared NPs was assessed by photodegradation of B19 and R76 dyes as industrial dye pollutants under visible light illumination. The degradation efficiency (η) was evaluated by equation (1) and the results are represented in figure 8. Different activity values for the photocatalysts of both dyes reveal that the PCA essentially hanged onto the dopant material used and increases by introducing the dopants into

Table 1. Particle size, energy gap, surface area and pore volume of the investigated samples.

Sample	Particle size (nm)	Energy gap (eV)	Surface area ($m^2 g^{-1}$)	Pore volume ($cm^3 g^{-1}$)
T	37	3.33	68 (65)	0.17 (0.15)
CT	31	3.16	86 (78)	0.27 (0.24)
ST	29	2.66	91 (84)	0.22 (0.20)
NT	24	2.36	113 (104)	0.29 (0.26)
CNST	20	2.18	127 (115)	0.37 (0.33)

Values within brackets are after five photocatalytic cycles.
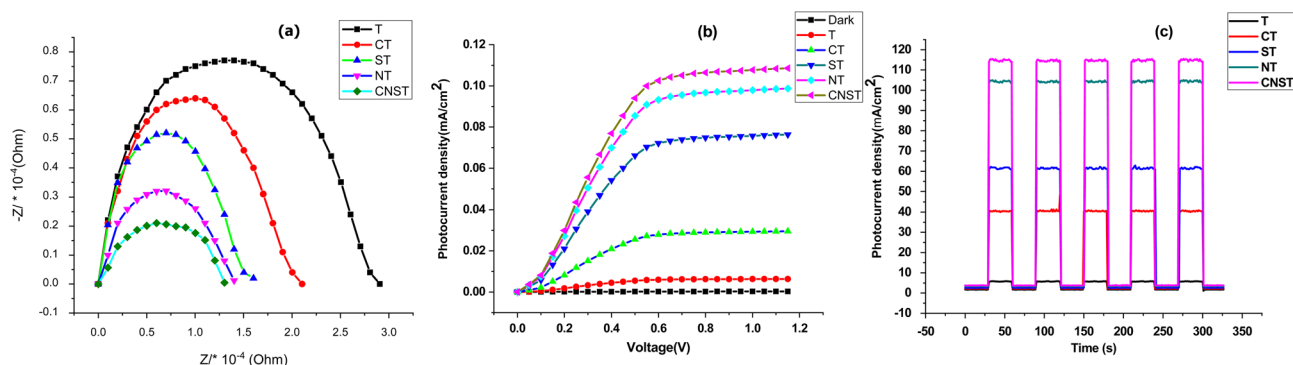
Figure 7. (**a**) EIS spectra of pure and doped TiO_2 NPs, (**b**) current–potential curves for photoelectrodes of the prepared pure and doped TiO_2 NPs and (**c**) the chronoamperometric currents at 0.5 V (*vs.* saturated calomel electrode) for the pure and doped TiO_2 NPs.
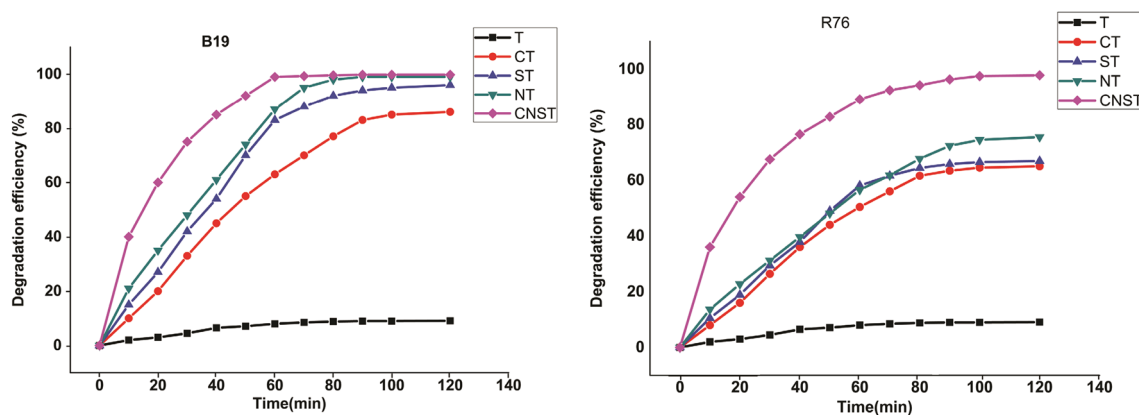
Figure 8. Photocatalytic efficiency of the pure and doped TiO_2 NPs for the degradation of B19 and R76 dye solutions.

TiO_2 in the order: CNST > NT > ST > CT > T. The superior PCA of CNST among all other samples could be attributed to its higher surface area and lower E_g.

It is worth mentioning that the dye solutions are very stable and, in the absence of photocatalysts, no decomposition can be observed under the same experimental conditions as the photocatalysts used.

Several parameters affecting the rate of PCD, therefore, the reaction variables like initial dye concentration, catalyst loading and solution pH were optimized to realize higher degradation efficiency.

The explanation of the pH influence on the photocatalytic degradation process occurring at the catalyst surface is complicated because it includes several factors, such as oxidation potential of the valence band, charge of catalyst surface and other physio-chemical properties. In the present study, the role of pH on the rate of PCD of the investigated dyes was studied by keeping all other experimental conditions constant and varying the initial pH values from 1 to 11 with hydrochloric acid or sodium hydroxide. The results given in figure 9 show an increase in the PCA of the photocatalysts towards both organic dyes
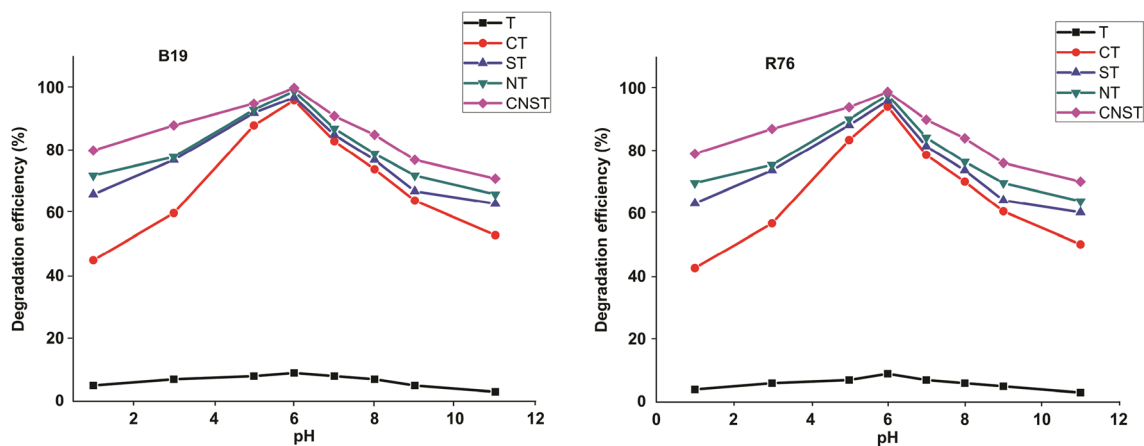
Figure 9. pH effect on the degradation of reactive blue 19 (B19) and reactive red 76 (R76) dye solutions over the pure and doped TiO_2 NPs.
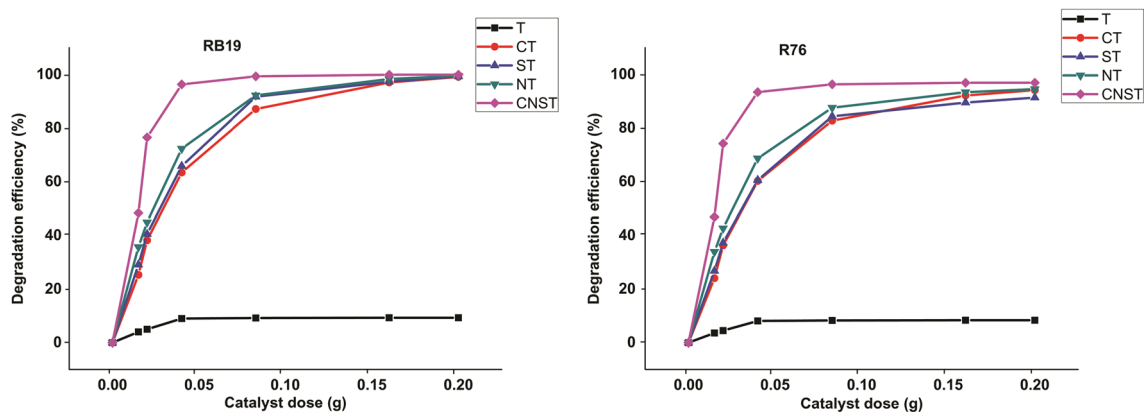
Figure 10. Effect of catalyst dosage of pure and doped TiO_2 NPs on the degradation of reactive blue 19 (B19) and reactive red 76 (R76) dye solutions.

with the change of pH and reach a maximum value at pH = 6.

The effect of amounts of the as-prepared photocatalysts on efficient B19 and R76 dyes degradation was investigated. In the present study, the amount of photocatalyst was varied from 10 to 20 mg for 50 ml of wastewater concentration of 10 ppm at pH 6 for 2 h. The rate of degradation was found to increase with the increase in catalyst loading and attains slight value change after 0.05 g catalyst dosage for the tested samples (figure 10).

To determine the main active species produced in the photocatalytic process, several quencher materials were injected into 10 ppm aqueous dye solution and 0.1 g CNST as a template for the photocatalyst studied. Triethylamine, isopropanol, carbon tetrachloride and benzophenone have been used as e^-, $^\bullet OH$, $^\bullet O_2^-$ and h^+ scavengers, respectively. The results represented in figure 11 show that the scavengers were able to inhibit the degradation rate and the highest PCD of the dyes was noted in the nonexistence of any quencher because all produced photoreactive species

contributed to the PCD process. Figure 11 also shows low PCA in the presence of each one of the scavengers added according to the order: $h^+ > {}^\bullet OH > {}^\bullet O_2^- > e^-$. This assures that the h^+ is the most important species in the present photocatalytic process. The peroxide radical ($^\bullet O_2^-$) anions formed in the photocatalytic oxidation process are obtained from the interaction between the emitted e^- from the VB to CB of photocatalyst through the irradiation process and O_2 molecule [38].

To evaluate the stability of the investigated catalysts under visible light irradiation, the catalytic samples were recovered after five cycles and re-evaluated with XRD and BET techniques, and the data obtained are given in supplementary figures S3 and S4 and table 1. The results show a decrease in the BET surface area accompanied by an increase in the XRD peak suggesting that the crystallinity of the samples has been changed. CNST photocatalyst showed the best PCA, thus its stability was studied. The renewal of the photocatalyst was done by filtration, washing three times with ethanol, then, distilled water and finally drying in
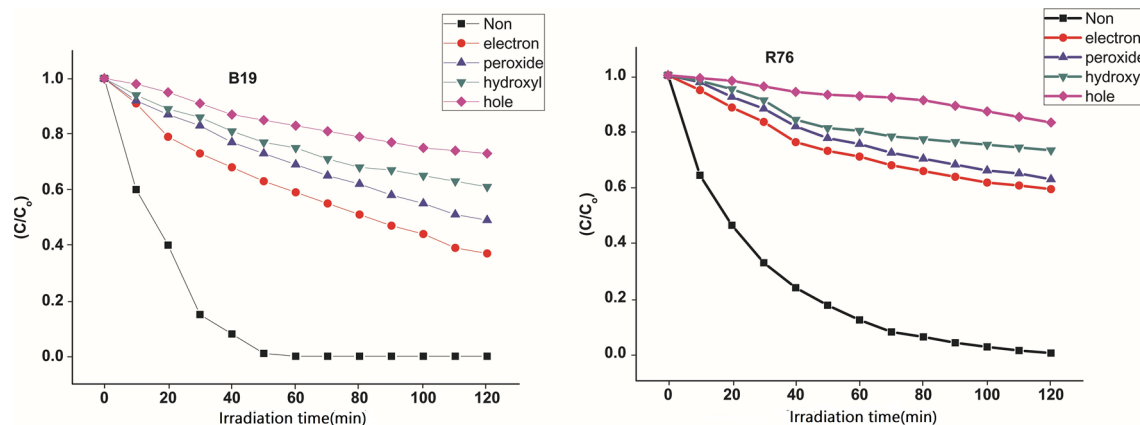
Figure 11. Scavenger effect on the degradation rate of reactive blue 19 (B19) and reactive red 76 (R76) over the pure and doped TiO_2 NPs.
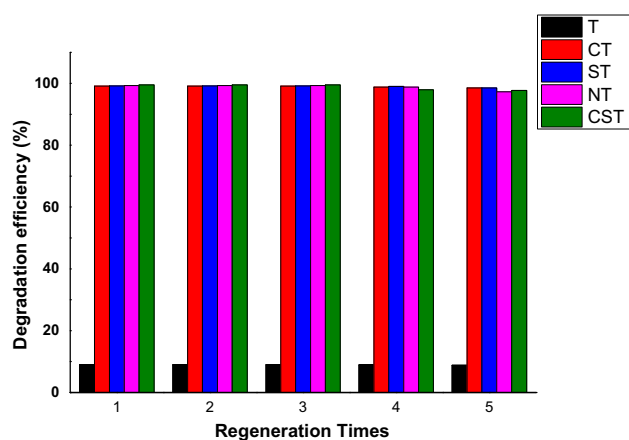
Figure 12. Degradation efficiency of the pure and doped TiO_2 NPs through five cycles.

an oven at 110°C. Stability investigations were done by repeating the photocatalytic reaction five times using the regained photocatalyst and the results acquired (figure 12) show that there is no clear reduction in PCA up to the third cycle. The slight decrease observed in the photodegradation efficiency of the B19 dye can be attributed to a blockage of photocatalytic active sites as a result of the strong adsorption of the dye intermediates on the photocatalyst surface [38].

COD test was used to estimate the organic dyes loaded in the wastewater level. The COD value of untreated wastewater decreases from 282 mg l^{-1} to lower values by

using the photocatalysts (table 2); it reaches 1.4 mg l^{-1} for the highest PCA sample with a composition of CNST.

4. Conclusions

In the present investigation, pure TiO_2 and non-metals doped TiO_2 (CT, ST, NT and CNST) NPs with anatase structure were prepared by using a sol–gel method in an aqueous extract of mangrove plant leaves and characterized using different techniques. The PCD of the B19 and R76 industrial dyes over the prepared catalysts under visible light irradiation show higher activity for the doped samples than that of the undoped one. This is explained based on the spectral response in the visible light region and the creation of intermediate energy levels leading to decrease in the E_g of TiO_2 by non-metal doping and photo-induced carriers' rapid separation through the dopant elements. Among the doped NPs, the CNST shows the highest photocatalytic performance, it is believed to develop from the synergic effect of carbon, nitrogen and sulphur, and the small crystallite size, high specific surface area (127 m^2 g^{-1}), and large pore volume (0.37 cm^3 g^{-1}). Besides the highest activity of the CNST, it also shows high stability during photocatalytic degradation of the dye's solution investigated. This approach opens up new pathways for the preparation of novel photocatalysts with several applications to increase the removal of a huge amount of organic wastes from wastewater that drained

Table 2. COD values reported for the wastewater and treated wastewater using T, CT, ST, NT and CNST.

Samples	Untreated wastewater	Treated wastewater using				
		T	CT	ST	NT	CNST
COD values (mg O_2 l^{-1})	282	210	44.8	26	15.6	1.4
η after treatment	0	25.5	84.1	90.7	94.4	99.5

every day from the chemical factories, textile and other industries.

References

[1] Fang Bai Li A B, Li X Z and Cheah K W 2005 *Environ. Chem.* **2** 130

[2] Patra A K, Kundu S K, Bhaumik A and Dukjoon Kim D 2016 *Nanoscale* **8** 365

[3] Bera R, Kundu S and Patra A 2015 *ACS Appl. Mater. Interfaces* **7** 13251

[4] Lavand A B and Malghe Y S 2015 *Adv. Mater. Lett.* **6** 695

[5] Gomes J, Lincho J, Domingues E, Quinta-Ferreira R M and Martins R C 2019 *Water* **11** 373

[6] Ge J, Zhang Y, Heo Y and Park S 2019 *Catalysts* **9** 122

[7] Nasr M, Eid C, Habchi R, Miele P and Bechelany M 2018 *ChemSusChem* **11** 3023

[8] Ma Y, Wang X, Jia Y, Chen X, Han H and Li C 2014 *Chem. Rev.* **114** 9987

[9] Wang C, Zeng T, Zhu S and Gu C 2019 *Appl. Sci.* **9** 339

[10] Valentin C D and Pacchioni G 2013 *Catal. Today* **206** 12

[11] Maletić M, Vukčević M, Kalijadis A, Janković-Častvan I, Dapčevic A, Laušević Z *et al* 2019 *Arab. J. Chem.* **12** 4388

[12] Challagulla S and Roy S 2017 *J. Mater. Res.* **32** 2764

[13] Mutuma B K, Shao G N, Kim W D and Kim H T 2015 *J. Colloid Interface Sci.* **442** 1

[14] Ramakrishnan V, Natarajan M, Santhanam A, Asokan V and Velauthapillai D 2018 *Mater. Res. Bull.* **97** 351

[15] Ashok C H, Rao K V, Chakra C H and Rajendar V 2015 *Int. J. Multidiscip. Adv. Res. Trends* **2** 241

[16] Lusvardi G, Barani C, Giubertoni F and Paganelli G 2017 *Materials* **10** 1208

[17] Gautam G, Saxena G, Singh V, Yadav A, Bhargava R and Thapa K 2018 *Chem. Eng. J.* **336** 386

[18] Dara S S 1999 *A textbook on experiments and calculations in engineering chemistry* (New Delhi: S. Chand Publication)

[19] Klug H and Alexander L 1974 *X–ray diffraction procedure for polycrystallite and amorphous materials* 2nd edn (New York: John Wiley and Sons)

[20] Bezrodna T, Puchkovska G, Shymanovska V, Baran J and Ratajczak H 2004 *J. Mol. Struct.* **700** 175

[21] Rahimi R, Moghaddam S S and Rabbani M 2012 *J. Sol–Gel Sci. Technol.* **64** 17

[22] Hua Xu J, Dai W, Li J, Cao Y, Li H, He H *et al* 2008 *Catal. Commun.* **9** 146

[23] Shi Y and Zuo J 2011 *Adv. Mater. Res.* **183** 1842

[24] Li Q, Zhang Z, Zhang K, Xu L, Fang J, Lai Y *et al* 2013 *J. Solid State Electrochem.* **17** 2959

[25] Bezerra P, Cavalcante R, Garcia A, Wender H, Martines A, Casagrande G *et al* 2017 *J. Braz. Chem. Soc.* **28** 1788

[26] Tauc J 1974 *Amorphous and liquid semiconductors* (London: Plenum)

[27] Meng Ni, Leung K, Dennis Y and Sumathy K 2007 *Renew Sustain. Energy Rev.* **11** 401

[28] Peng F, Cai L, Yu H, Wang H and Yang J 2008 *J. Solid State Chem.* **181** 130

[29] Jiang X, Manawan M, Feng T, Qian R, Zhao T, Zhou G *et al* 2018 *Catal. Today* **300** 12

[30] Fang M, Chen Z X, Wang S Z and Lu H B 2012 *Nanotechnology* **23** 1262

[31] Xu J H, Li J, Dai W, Cao Y, Li H and Fan K 2008 *Appl. Catal. B: Environ.* **79** 72

[32] Zong H, Zhao T, Zhou G, Qian R, Feng T and Pan J 2019 *Catal. Today* **335** 252

[33] Reddy P, Reddy P, Sharma V, Srinivas B, Kumari V and Subrahmanyam M 2010 *J. Water Resour. Prot.* **2** 235

[34] Liu S and Chen X 2007 *J. Hazard. Mater.* **152** 48

[35] Baram N and Ein-Eli Y 2010 *J. Phys. Chem. C* **114** 9781

[36] Kang X, Liu S, Dai Z, He Y and Song X 2019 *Catalysts* **9** 191

[37] Zhou M and Yu Y 2008 *J. Hazard. Mater.* **152** 1229

[38] Lin Y M, Li D Z, Hu J H, Xiao G C, Wang J X, Li W J *et al* 2012 *J. Phys. Chem. C* **116** 5764